First observations of CH_4 and H_3^+ spatially-resolved emission layers at Jupiter equator, as seen by JIRAM/Juno

A. Migliorini[1], B.M. Dinelli[2], C. Castagnoli[1,2,3], M.L. Moriconi[1], F. Altieri[1], S. Atreya[4], A. Adriani[1], A. Mura[1], F. Tosi[1], A. Moirano[1], G. Piccioni[1], D. Grassi[1], R. Sordini[1], R. Noschese[1], A. Cicchetti[1], S.J. Bolton[5], G. Sindoni[6], C. Plainaki[6], A. Olivieri[6]

[1]IAPS-INAF, Istituto di Astrofisica e Planetologia Spaziali, Rome, Italy.

[2]CNR-ISAC, via Gobetti 101, 40129, Bologna, Italy

[3]University of Tor Vergata, via della Ricerca Scientifica 1, 00133, Rome, Italy

[4]Dept. of Climate and Space Sciences and Engineering, University of Michigan, Ann Arbor, Michigan, USA

[5]Southwest Research Institute, San Antonio, Texas, USA

[6]Agenzia Spaziale Italiana, via del Politecnico snc, 00133, Rome, Italy

Key Points:

- Detection of CH_4 and H_3^+ emissions over Jupiter's disc, as two well separated layers in the equatorial region at 200 km and 600 km.
- H_3^+ spectral signatures can be reproduced by retrieving the temperature or its Volume Mixing Ratio (VMR) and temperature simultaneously.
- The H_3^+ temperature profile shows a peak of 600-800 K at about 600 km with some differences with respect to the Galileo's profile.
- The observed features point out the presence of localised variability with altitude, perhaps indicative of wave activities.

Corresponding author: Alessandra Migliorini, alessandra.migliorini@inaf.it

Abstract

In this work we present the detection of CH_4 and H_3^+ emissions in the equatorial atmosphere of Jupiter as two well separated layers, located, respectively, at tangent altitudes of about 200 km and 500-600 km above the 1-bar level using the observations of the Jovian InfraRed Auroral Mapper (JIRAM), on board Juno. This provides details of the vertical distribution of H_3^+ retrieving its Volume Mixing Ratio (VMR), concentration and temperature. The thermal profile obtained from H_3^+ shows a peak of 600-800 K at about 550 km, with lower values than the ones reported in Seiff et al. (1998) above 500 km using VMR and temperature as free parameters, and above 650 km when VMR is kept fixed with that model in the retrieval procedure. The observed deviations from the Galileo's profile could potentially point to significant variability in the exospheric temperature with time. We suggest that vertically propagating waves are the most likely explanation for the observed VMR and temperature variations in the JIRAM data. Other possible phenomena could explain the observed evidences, for example, dynamic activity driving chemical species from lower layers towards the upper atmosphere, like the advection-diffusion processes, or precipitation by soft electrons, although better modelling is required to test these hypothesis. The characterisation of CH_4 and H_3^+ species, simultaneously observed by JIRAM, offers the opportunity for better constraining atmospheric models of Jupiter at equatorial latitudes.

Plain Language Summary

The Jovian Infrared Auroral Mapper (JIRAM) is the infrared (IR) imager and spectrometer on board the Juno mission, designed to investigate Jupiter's atmosphere. A key objective of JIRAM is the investigation of the minor species, like CH_4 and H_3^+ that are very important to understanding the energy balance of the middle and upper atmosphere of Jupiter. These species have strong signatures in the 3.3-3.8 μm spectral region, well within the nominal wavelength range of the instrument. We present the analysis of recent images and spectra obtained by JIRAM, in the period December 2018 to September 2020, plus additional measurements in March 2017, to study methane and H_3^+ vertical distribution at equatorial latitudes. We find that CH_4 is localised around 200 km above the 1-bar level, while a distinct layer of H_3^+ is observed around 500-600 km (0.04-0.016 microbar). The observed vertical distribution and intensity variation of H_3^+ is likely to be the result of vertically propagating waves. However, other possible phenomena can

be invoked to explain these findings, like for example an uplifting of chemical species from lower layers towards the upper atmosphere, or soft electrons precipitation, although a rigorous modelling is needed to confirm the latter hypothesis.

1 Introduction

The thermosphere/ionosphere and stratosphere of Jupiter are populated by atoms and molecules, which include H, H_2, H_3^+ and CH_4. Among the molecules, CH_4 has a strong solar pumped non-local thermodynamic equilibrium (non-LTE) emission centred at 3.3 μm, while H_3^+, produced either via solar or impact ionization, is in quasi-thermal equilibrium (q-LTE; (Miller et al., 1990)) emitting from a large number of lines in the band 2-5 μm. H_3^+ infrared (IR) emission lines are used to evaluate the atmospheric and satellite interaction with energetic particles, which deposit energy in the upper atmosphere of Jupiter especially in the auroral region (Kim et al., 1985; Connerney et al., 1993; Clarke et al., 2002; Mura et al., 2017, 2018; Gèrard et al., 2018) and are also known to have a cooling effect on the atmosphere (Bougher et al., 2005; Koskinen et al., 2007; Stallard et al., 2017). Several H_3^+ emission lines, mainly due to the fundamental ν_2 band (Drossart et al., 1989; Giles et al., 2016), have been identified in the auroral region as well as at mid-equatorial latitudes (Miller et al., 1997; Ballester et al., 1994; Stallard et al., 2015; Migliorini et al., 2019). In particular, the wavelength region around 3.4 μm can be exploited to study the auroral emissions due to H_3^+, because of its numerous and intense emission lines that can be identified above a deep methane absorption band within the underlying atmosphere. A thorough review of H_3^+ observations and properties for the giant planets can be found in Miller et al. (2020), while a new modelling interpretation strategy is reported in Moore et al. (2019).

The intensity of the H_3^+ emission at mid and equatorial latitudes is about 10 times fainter than in the auroral region (Ballester et al., 1994; Marten et al., 1994; Stallard et al., 2018) and it is produced in-situ by solar ionization of molecular hydrogen. An optically thin layer of H_3^+ at the equator was clearly identified in the images acquired by the ProtoCAM infrared camera mounted on the Infrared Telescope Facility (IRTF), located at 700-750 km above the 600 mbar-level (Satoh & Connerney, 1999). More recently, a map of the H_3^+ emission in the region between $\pm 60°$ in latitude was obtained using the data acquired at the NASA Infrared Telescope Facility, covering overall a period of 48

nights (Stallard et al., 2018). The same measurements revealed a dark ribbon within 15° of the jovigraphic equator, which is indicative of the magnetic equator of Jupiter.

Emissions at 3.3 μm due to methane were identified for the first time using the NASA Infrared Telescope Facility (Kim et al., 1991) at the North polar region, while a bright small spot due to CH_4 was detected near the South pole in the same spectral region by Kim et al. (2009). However, methane brightening in the polar regions was well studied in the 8-μm band (Kim et al., 1985; Drossart et al., 1993), reporting different behaviours in the North (Caldwell et al., 1983; Sada et al., 2003) and the South (Caldwell et al., 1988). The methane bright spots have different morphologies at 3- and 8-μm, and this could be explained by the different altitudes where the emissions occur (Lystrup et al., 2008). In addition, recent auroral observations reported that northern and southern emissions imaged at 8-micron vary independently (J. A. Sinclair et al., 2017). High-resolution measurements in the 3.3-3.4 μm band pointed out that the observed methane molecules in the polar region are likely excited by energetic sources, possibly provided through auroral particle precipitation or Joule heating above the 1-μbar level (Kim et al., 2015), although further observations are required to discriminate between the two processes.

Faint emissions due to methane around 3.3 μm have been observed by the spectrometer embedded into the Jovian Infrared Auroral mapper (JIRAM) on board the Juno mission, in the polar regions, localized within the main auroral oval (Adriani et al., 2017b; Moriconi et al., 2017) and with the Near Infrared Mapping Spectrometer (NIMS) on the Galileo spacecraft (Altieri et al., 2016). In the ultraviolet (UV), few signatures due to CH_4 were identified using the Ultraviolet Spectrograph (UVS) instrument on Juno (Bonfond et al., 2017). Other complex hydrocarbons, such as C_2H_4, C_3H_4 and C_6H_6 have been observed in the auroral regions of Jupiter (Kim et al., 1985; J. Sinclair et al., 2019).

Models predict the intensities and vertical distribution of both H_3^+ and methane (Grodent et al., 2001; Kim et al., 2014). Direct H_3^+ vertical profile measurements have been reported for the Southern auroral region, using NIRSPEC spectrometer observations on the Keck II telescope (Lystrup et al., 2008), showing a good agreement with models for ion densities; however, the measured exospheric temperature of 1450 K was about 150 K higher than predictions. More recent observations with the Infrared Camera and Spectrometer (IRCS) at the Subaru 8.2 m telescope allowed reconstructing the vertical profile of H_3^+ overtone and hot overtone, located at different altitudes, at 700-900 km and

680-950 km above the 1-bar level, respectively (Uno et al., 2014). Further measurements in L- and K- bands using the IRCS at Subaru allowed a comparison between the horizontal and vertical profiles of H_3^+ fundamental and overtone emission lines (Kita et al., 2018). Observations confirmed the previous findings reported in Uno et al. (2014) and also showed that the fundamental emission line has a peak altitude at 650±100 km, lower than what obtained for the overtone lines, but overall consistent with theoretical models. While direct measurements have been reported for the H_3^+ vertical profile, at auroral and mid-equatorial latitudes (Miller et al., 1997; Ballester et al., 1994; Stallard et al., 2015; Migliorini et al., 2019; Dinelli et al., 2019), information for the CH_4 vertical distribution at equatorial latitudes is missing due to the emission faintness observed during the reported observations. Recently, JIRAM, on board the Juno spacecraft, performed a dedicated limb observation campaign, starting from 24 May 2018 (perijove passage 13, PJ13). The high sensitivity of JIRAM and the capability to measure both images and spectra in the 3-4 μm spectral range allowed the detection of the infrared emissions due to both CH_4 and H_3^+ close to the equator. In the present paper, we discuss the results obtained in the analysis of JIRAM limb observations, exploiting both images and spectra acquired during the Juno mission period December 2018-September 2020 (i.e. perijove passages 17 to 29), complemented with spectra, acquired over Jupiter limb in March 2017 (perijove passage 5), in the equatorial region. The paper is organised as follow: the data are presented in section 2, the description of the results in section 3. Discussion is provided in section 4, while conclusions are summarised in section 5.

2 Observations and data selection

2.1 Instrument description

JIRAM, onboard the Juno mission, combines an imager and a spectrometer in the same instrument (Adriani et al., 2017a). The imager is composed of two broad-band filters, centred at 3.45 μm (L-band, bandpass 3.3-3.6 μm) and 4.85 μm (M-band, bandpass 4.5-5.0 μm), respectively, located in the same detector, which has a total dimension of 256 x 432 pixels, 256 being the number of lines and 432 the number of samples. The Instantaneous Field of View (IFOV) of each pixel is 0.01° which implies a FOV of 5.87°x1.74° for each band of the imager. The spectrometer covers the 2-5 μm spectral region, with a spectral sampling of about 9 nm; it is composed of a 256-pixels slit, and each pixel is expanded into 336 spectral channels, concurrently acquired. The spectral

slit is located within the M-band filter, and simultaneously commanded with the imager. However, due to the spinning movement of the spacecraft Juno, the JIRAM spectrometer is not able to acquire contiguous slit images of the target. This means that it is not possible to reconstruct the full scene observed by the imager at the same time. However, although with a sparse coverage, the observed spectra can be exploited to quantitatively study the distribution of CH_4 and H_3^+. In case of limb measurements, the spectrometer enables the atmosphere to be sampled at different altitudes along the line of sight above the 1-bar level, using the pixels located outside the disk of the planet. More details of the observations are provided in the following sections. The orbit attitude of the Juno spacecraft allowed the routine observation of the equatorial region starting from orbit 13, while only sparse measurements are available during the previous orbits. In the present work, we include the analysis of images and spectra acquired during the perijove (PJ) passages 17 to 29 (December 2018 to September 2020), and a spectral sequence acquired during PJ 5 (March 2017). Details of the analyzed images and spectra are provided in the sections 2.2 and 2.3, respectively.

2.2 JIRAM imager data and their analysis

In the limb campaign started with the orbit 13 (May 2018), a total of 89 images have been acquired by JIRAM. However, most of the data, especially during PJs 13, 14, 15, 16, and 19, were strongly contaminated by environmental radiation, and could not be used in the analysis. Hence, in this work we use only data with a good signal-to-noise ratio and minimally affected by radiations, visually selected among those including at least partly the limb of the planet. The list of the images included in the present analysis is provided in Table A1. The ranges of System III planetocentric geographical latitude and longitude covered with each image are reported.

Two examples of full JIRAM raw images are shown in Figure 1. It is possible to see the environmental radiation distributed across the whole image in the form of dark and bright pixels randomly distributed. This affects more the L-band image, while lower radiation contamination is observed in the M-band image because in this part of the detector the signal is several orders of magnitude larger than in the L-band part, making the radiation induced signal much smaller compared to the signal. In the case shown in Figure 1a, the radiation effect is not so strong as to conceal the underlying emission pattern and therefore the image has been retained in the analysis. The radiation effect in

the image shown in Figure 1b is more dramatic, and hence JIRAM images like this one are not included in the analysis. In Figure 2 we reconstruct the tangent altitude of the L-band image shown in Figure 1a, which is defined as the minimum altitude reached by the line of sight (LOS) of each pixel. The yellow line located at the right edge of the image (see Figure 2) indicates the location of the 1-bar level of Jupiter's atmosphere, while the red dashed line on the left indicates the tangent altitude at 1000 km above that level. Two layers are clearly visible in the image, the strongest one located closer to the 1-bar level and a fainter diffuse layer above it. To infer the altitude of the two emission layers, a best-fit algorithm is applied. For each pixel of the data image (JIRAM-IMA), the line of sight is derived from SPICE kernels (Acton, 1996), and its contribution from different altitudes is evaluated. The reconstructed image (Figure 2b) is then simulated by integrating the vertical profile along the line of sight. The resulting image is compared with the original data and the vertical profile is tuned until the best match is obtained (Figure 3). The reconstructed image differs from the original data by less than 5% and, considering that the pseudo-inverse matrix procedure is a linear operator, this percentage could be assumed as an upper limit for the uncertainty of the vertical profile. In Figure 3 we show the result of the above-described method: the vertical profile of the emissions intensity shows two maxima, one at about 200 km, and one around 650 km. We attribute the first maximum to the methane emission and the second one to the H_3^+ emission. The error bars are calculated assuming a 5% uncertainty, as previously explained. This procedure can only be applied to the JIRAM imager channel measurements, as the best-fit algorithm requires a large number of pixels to converge to a physical solution. For the spectrometer, only the tangent altitude can be used. When plotting the raw imager data (Figure 2), the secondary peak is at about 550 km from the planetary limb (i.e. the tangent altitude of the peak is 550 km), while we know that this emission is actually about 100 km higher, as obtained with the inversion method. This implies that using the tangent altitudes of the spectrometer data to calculate the vertical profile leads to an underestimation of the altitude of up to 100 km, which must be taken in consideration.

The images included in this analysis cover the planetocentric latitude region from 53°S to 42°N. Most of the images are acquired at longitudes 110-240 W, with few measurements covering the ranges 30-70 W and 290-330 W (Table A1). Geometric informa-

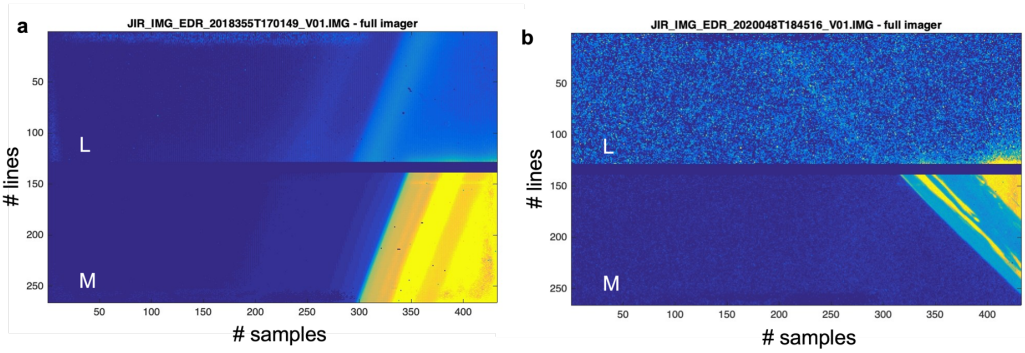

Figure 1. Example of JIRAM image (JIRAM-IMA) at limb. a: Full JIRAM-IMA, showing the L-band acquisition in the top and the M- one at the bottom, affected by a low radiation. This example refers to 6 S and 200 W. b: Another example of JIRAM-IMA at limb highly affected by radiation and not included in the analysis. This image refers to 38 S and 224 W.

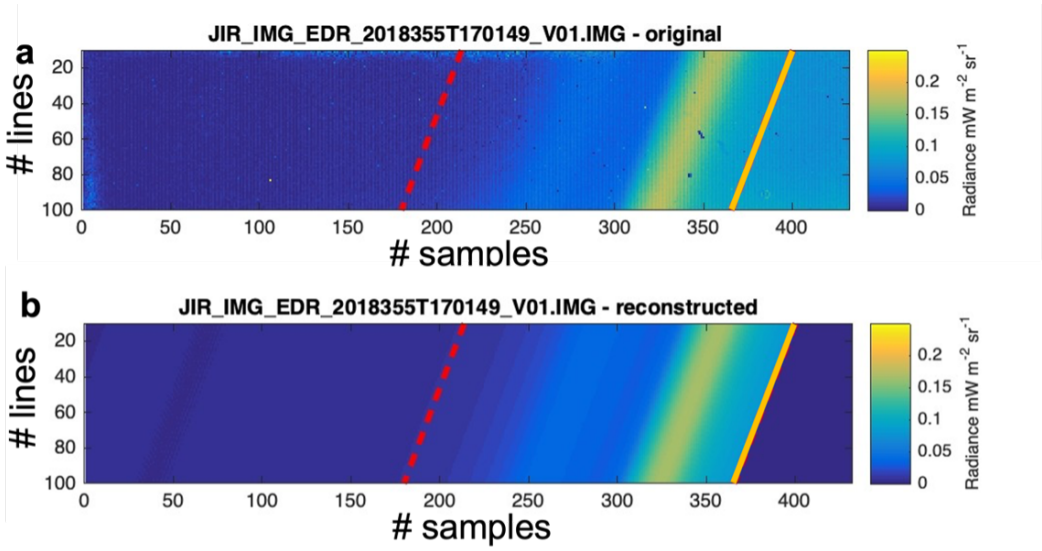

Figure 2. a: Same L-band JIRAM-IMA shown in Figure 1a, where the color coding indicates radiance. The yellow and red lines indicate the 1-bar level and 1000 km above it, respectively. b: Simulated image from the reconstructed vertical profile. The dark blue region at the bottom right, beyond the yellow line, represents the Jupiter 1-bar level surface.

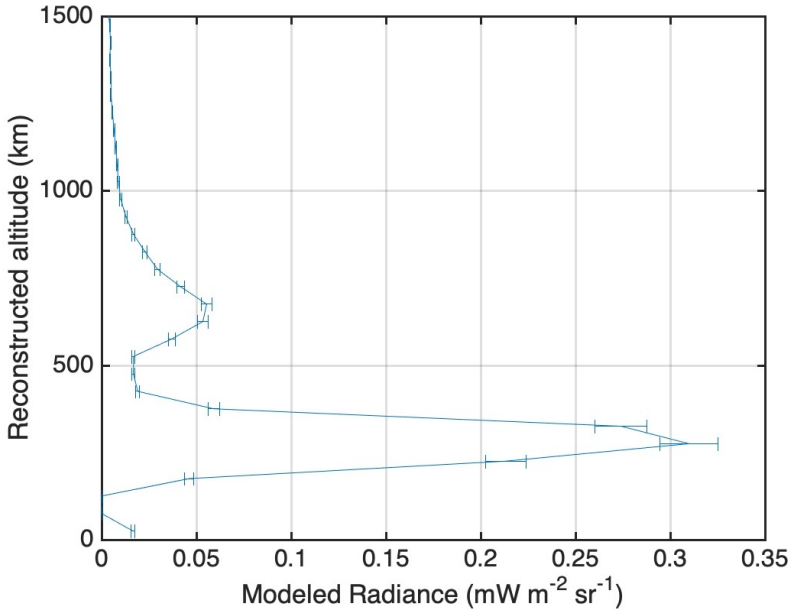

Figure 3. Reconstructed vertical profile for JIRAM-IMA shown in Figure 1a obtained using the inversion method. The y axis shows the reconstructed altitude, the x axis shows the modelled radiance. Uncertainty in the vertical profile is assumed to be the 5%, as explained in the text.

tion of each pixel in the images, including those pointing at the limb, have been calculated.

2.3 JIRAM spectral data and spectral radiance analysis

To confirm the findings obtained with the analysis of the JIRAM-IMAs and the assignment of the intensity peaks to either H_3^+ and CH_4, whose signatures are well resolved at JIRAM spectral resolution, spectra acquired simultaneously to the images have also been examined. Spectral limb sequences have been selected following Migliorini et al. (2019) and Dinelli et al. (2019). Each pixel of the spectrometer's slit, located outside the Jupiter's disk, samples the atmosphere over a range of altitudes above the 1-bar level, along the instrument LOS crossing the atmospheric shells, in which the atmosphere is ideally divided. We refer to the set of spectra acquired by the spectrometer in a single measurement session, relative to the pixels outside the Jupiter disk, as a limb sequence. The spectral acquisition of 21 December 2018 is shown in Figure 4, with the latitude distribution as a reference. It was originally composed of seven slit images, three of which pointing the deep space and hence not shown here.

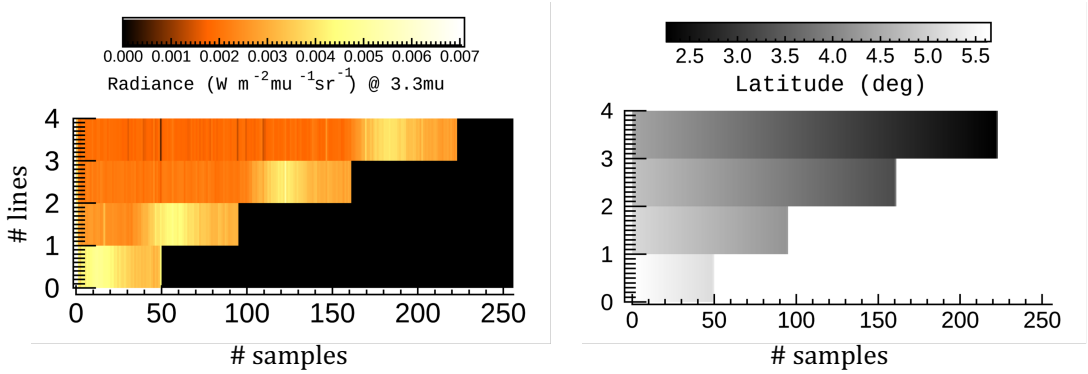

Figure 4. Spectral sequence of 21 December 2018. Radiance at 3.32 μm, expressed in W m^{-2} μm^{-1} sr^{-1}, is shown on the left for each slit image. The x-axis refers to the pixel along the slit, while the y-axis reports the temporal variation of the sequence (number of scans). The black region indicates the Jupiter's body masked at 1-bar level, as obtained from the reconstructed geometry. On the right side, planetocentric latitude values for the same image are shown.

Although limb measurements aligned along the vertical to Jupiter's 1-bar surface are not possible with the JIRAM spectrometer, due to pointing constraints, we verified that each pixel along the slit acquisition was scanning the atmosphere within 1 deg of latitude and longitude. For the dataset used in this work, 1 deg in terms of latitude and longitude corresponds to a box of about 1246 x 1244 km at a latitude of 4°. Since JIRAM spectra are affected by a sawtooth shape (odd-even pattern) due to the measurement strategy, the faint emissions due to both H_3^+ and CH_4 were in some cases hidden by the background noise. In practice, the radiance of an odd/even channel can be a little bit higher or a little bit lower than the average of the neighbor even/odd channels. For this reason, each spectrum has been corrected to attenuate, and in some cases remove, the odd-even pattern. The correction is based on the fact that the intensities of the odd and even channels of the spectrometer are consistently shifted, and show a sawtooth pattern, more pronounced in case of a low signal. In order to take this effect into account, two spline curves are fitted to the odd and even channels separately. Then the two splines are interpolated onto the original grid of spectral bands, which results in two separate spectra. These spectra are finally averaged to obtain the cleaned spectrum. This correction has allowed to recover spectra that were not used in the first analysis of JIRAM limb spectra (see Migliorini et al., 2019).

Table 1. Geometric parameters of the analysed spectra

# JIRAM section	Latitude (deg)	Longitude (deg)	Solar Zenith Angle
Limb 1	6 N	183 W	90
Limb 2	4 N	184 W	90
Limb 3	1.5 N	185 W	90

To test our hypothesis on the altitude of the CH_4 and H_3^+ emissions identified in the imager data, we investigated the selected spectral limb sequences, to reconstruct the vertical distribution of the two species separately in terms of radiance. Figure 5 shows the vertical distribution of the intensity of the CH_4 and H_3^+ emissions for the slit image on 21 December 2018 (3.8 N and 184 W, limb 2 in Table 1). The profiles are obtained considering the integrated intensity in the bands 3.29-3.34 μm (for CH_4) and 3.51-3.69 μm (for H_3^+), over altitude bins 100 km wide. The integrated radiances from the spectra with tangent altitude within the limits of each bin have been averaged and plotted with the standard deviation. The wavelength range for H_3^+ has been chosen to include the strongest H_3^+ bands observed in the spectra and avoid any contamination from other species or background noise. The averaged intensities have been corrected for the background (continuum) signal. It can be clearly seen in the figure that the JIRAM-IMA intensity peak at 200 km belongs to methane, while the other peak at about 500-600 km can be attributed to H_3^+.

In Figure 6 the JIRAM spectral profiles at different altitudes are presented for the case of data acquired on 21 December 2018. Each spectrum is obtained by averaging the data falling in the 100 km wide bins, for each spectral band. Dashed lines indicate the position of H_3^+ bands while the dotted line shows the position of the CH_4 band, at the wavelengths indicate in the upper panel of the image. As it can be seen, for altitudes below 350 km, the CH_4 band at 3.3μm is the strongest feature, while above 450 km H_3^+ becomes the dominant species.

2.4 Quantitative analysis of the spectra

The selected limb sequences have been analysed to retrieve the vertical distribution and temperature of H_3^+. Methane was initially included in the retrieval process, but

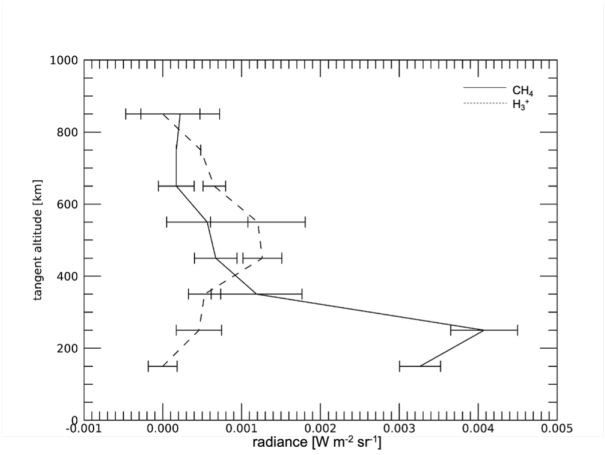

Figure 5. Vertical profile of integrated radiances for JIRAM spectral bands 3.29-3.34 μm and 3.51-3.69 μm, for CH_4 and H_3^+, respectively, in altitude bins 100 km wide. Data refer to JIRAM observation acquired on 21 December 2018.

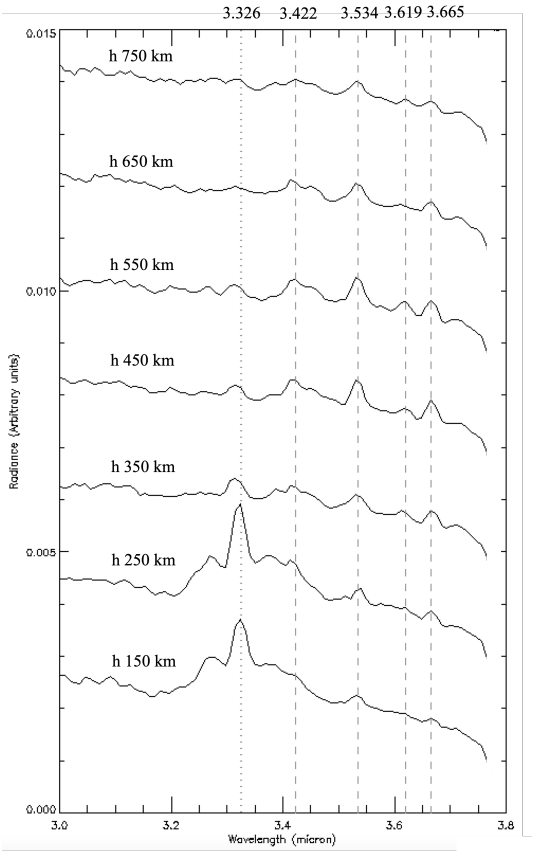

Figure 6. JIRAM spectra at different altitudes, obtained as average of the radiance in altitude bins 100 km wide. The dashed lines show the position of H_3^+ bands while the dotted line indicates the position of CH_4 band. Data refer to the spectral acquisition acquired on 21 December 2018 and shown in Fig. 4.

we did not obtain reliable results because a full treatment of the non-local thermodynamic equilibrium (non-LTE) is mandatory in case of this species, as demonstrated in Drossart et al. (1989); Kim et al. (2014); Sànchez-Lòpez et al. (2022). The latter authors demonstrated that the major contributors to the radiance at 3.3μm are the ν_3 and ν_3+ ν_4 levels of CH_4 which are in non-LTE at pressures lower than 10^{-1} mbar. The observed radiance, reported to be the result of CH_4 levels in non-LTE excited by the solar pumping action, is reproduced by using a full non-LTE model, which also takes into account the effects of the kinetic temperature profile and the collisional relaxation rates on non-LTE populations of the emitting states. In this way, the authors are able to obtain a better fit of the ISO/SWR Nadir data than what previously reported in Drossart et al. (1989); Kim et al. (2014). For this reason, the VMR and temperature values of CH_4 from the JIRAM data will be investigated in a future work, to include the non-LTE treatment.

Details of the retrieval process are provided in the following subsections. We have initially considered three limb scans, acquired during the sequence of observations on 21 Dec 2018, (shown in Figure 4), with the geometry parameters reported in Table 1. To confirm the results obtained by this first analysis, we have then included in the retrieval a set of 23 limb observations acquired on 27 March 2017 (PJ 5), originally used for the derivation of the H_3^+ distribution at equatorial and mid latitudes in Migliorini et al. (2019). The 23 sequences covered the latitude region from 5°S to 37°N, and the longitude interval from 102 W to 70 W. Even though the number of spectra and the vertical coverage and resolution of these limb sequences are very different from the ones acquired on 21 December 2018, a clear methane emission was visible at tangent altitudes below 300 km. Since the focus of the original work was the distribution of H_3^+ outside the auroral regions, the observations below 300 km were not included in the analysis reported in Migliorini et al. (2019). All the other limb observations used by Migliorini et al. (2019) were covering higher latitudes and no methane emission was visible.

2.4.1 Retrieval code and limb measurement

The measurements acquired with the spectrometer have been used to quantitatively retrieve the H_3^+ Volume Mixing Ratio (VMR) along with the temperature (T) and concentration. For the observations on 27 March 2017, only a few pixels sampled Jupiter's atmosphere above the limb. However, for the observations on 21 December 2018, more than 100 pixels sampled Jupiter's atmosphere above the limb, which resulted in a tan-

gent altitude separation of about 10 km. The retrieval code, which uses the global fit technique (Carlotti, 1988), and a Bayesian approach (optimal estimation Rodgers, 2000) with an iterative Gauss-Newton procedure, is the same used in Migliorini et al. (2019) and Dinelli et al. (2019). The Forward Model (FM), inside the retrieval code, numerically solves the integral of the radiative transfer along the instrument LOS in a curved atmosphere. The spectrum is computed with a line-by-line procedure. The simulation of more than 100 spectra has been proven to be too expensive in terms of computing time and memory allocation, therefore, we decided to divide the vertical extension of each slit measured in 2018 into bins of 50 km and to average all those spectra (typically 8) whose tangent altitudes fell into the bin. This reduced the number of spectra to be analysed for each slit and improved the S/N ratio of the observations. To avoid contamination of anomalous signals (i.e. spikes due to radiation) in the final average, we used the median instead of the mean value of the observed radiances at each wavelength. In the forward model inside the retrieval code, Jupiter's atmosphere is assumed vertically inhomogeneous and composed of curved layers (equidistant from Jupiter 1-bar surface) homogeneous in the horizontal direction only. This implies that its composition, pressure and temperature are allowed to vary with altitude within each layer. The simulation of the spectra is performed on a very fine frequency grid (0.0005 cm^{-1}), to take correctly into account all the emission and absorption processes of the single spectral lines. The high-resolution spectra are then convolved with the JIRAM instrumental response function (IRF, a gaussian) and the Field of View response function. The odd-even correction, implemented in the same way as for the measurement treatment reported above, is finally applied to the simulated spectra. The derivatives of the spectra with respect to the volume mixing ratio (VMR Jacobians) are analytically computed at the same time of the spectrum and convolved with the JIRAM IRF and corrected for the odd-even effect, while the temperature Jacobians are numerically computed. In the simulations, we assume Jupiter's atmosphere is made of H_3^+ and methane only, since all other molecules have small or negligible signal in the considered spectral region. The pressure values at the altitude above the 1-bar level are taken from Seiff et al. (1998).

Even though the FM can represent deviations from the LTE conditions, in our analyses, H_3^+ is assumed in LTE at the considered altitudes (see for example Melin et al. (2005), Grodent et al. (2001) and Tao et al. (2011)). Therefore, the retrieved temperatures reported in this analysis must be considered as effective values.

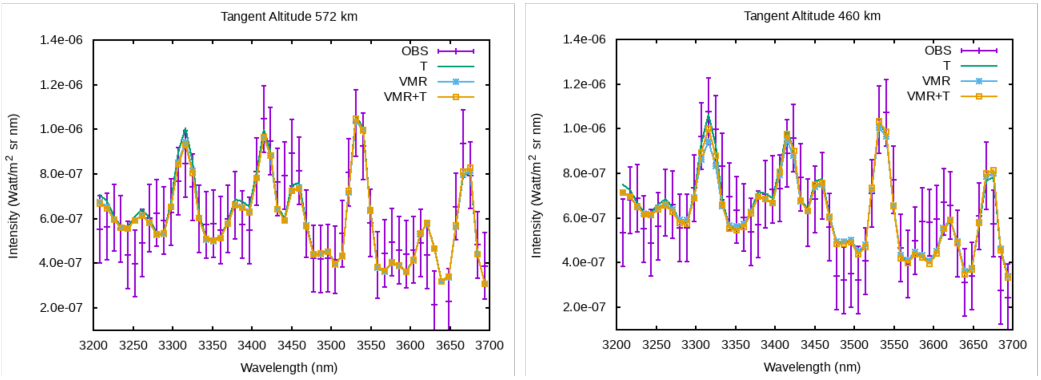

Figure 7. Examples of the limb spectra measured by JIRAM in the altitude range where only H_3^+ emissions are present The purple lines represent the measurements with their noise, the simulated spectrum at the end of the retrievals is represented by the green line when only T is retrieved, by the light blue line when only the VMR is retrieved, and by the yellow line when both T and VMR are retrieved.

The retrieval process is applied to the spectral region from 3.2 to 3.8 μm, because in this range, above 450 km, the spectrum is dominated by the H_3^+ alone, while solar scattering is so weak that it can be safely neglected. On the other hand, the treatment of the scattering by particles and molecules, which are important outside this range, is not included in the FM internal to the retrieval code. In Figure 7 two spectra observed by JIRAM in the altitude range dominated by the H_3^+ emissions are shown. JIRAM observations are represented by the purple points and the associated error bars represent the measurement noise of JIRAM. In the analyzed spectral region some of the lines of H_3^+ are almost superimposed to the Q-branch of methane (from 3.28 to 3.35 μm). When attempting the retrieval over the whole vertical coverage of the limb sequences, strong correlations between the H_3^+ and CH_4 vertical distributions are found. To avoid them, we restricted the retrieval of the vertical distributions of H_3^+ temperature and VMR in the vertical region from 450 to 800 km using the spectra with tangent altitudes above 400 km. Indeed, the behaviour of the spectral features at the different altitudes clearly showed that the emission recorded in the region above 400 km was only due to H_3^+, as also demonstrated in Figure 6, while the spectra at lower altitudes were dominated by the methane emission (not included in the present analysis).

The vertical distributions of temperature and VMR of the H_3^+ ions are free parameters that are obtained by our retrieval code, which works on a vertical grid with uni-

Table 2. A-priori profiles for the retrieved quantities

Altitude	H_3^+ VMR (ppmv)	Temperature (K)
800	0.4184E-01	877.2
750	0.3493E-01	826.0
700	0.2566E-01	741.0
650	0.1927E-01	686.5
600	0.1353E-01	669.8
550	0.7785E-02	653.2
500	0.2042E-02	545.9
450	0.1541E-02	509.4
400	0.1040E-02	370.2
350	0.9012E-03	265.1
300	0.8501E-03	227.6
250	0.8447E-03	203.3
200	0.8447E-03	208.2
150	0.8447E-03	214.6
100	0.8477E-03	208.0

form resolution of 50 km. In addition, a constant wavelength shift, also a free parameter of the retrieval process, is applied to account for possible second order calibration errors of the wavelength. Any other instrumental effect, which can contribute as an offset to the spectrum, was evaluated in the portions of the spectra which are free from molecular emissions and just a scaling factor was retrieved. The same a-priori and initial guess profiles were used for all the analyses, in order to ensure that the observed variability was real and not related to a variable a-priori/initial guess information. The a-priori profile for temperature was the one recorded by the Galileo probe and reported by Seiff et al. (1998) and was also used as initial guess in the vertical range from 400 to 800 km. H_3^+ and temperature a-priori profiles are reported in Table 2 and in Figure 8 for a better visualization. The a-priori errors for temperature and VMRs were assumed to be equal to 100 K and 100%, respectively H_3^+ spectroscopic data are the ones available at the web site `http://h3plus.uiuc.edu/database/` (Lindsay & McCall, 2001).

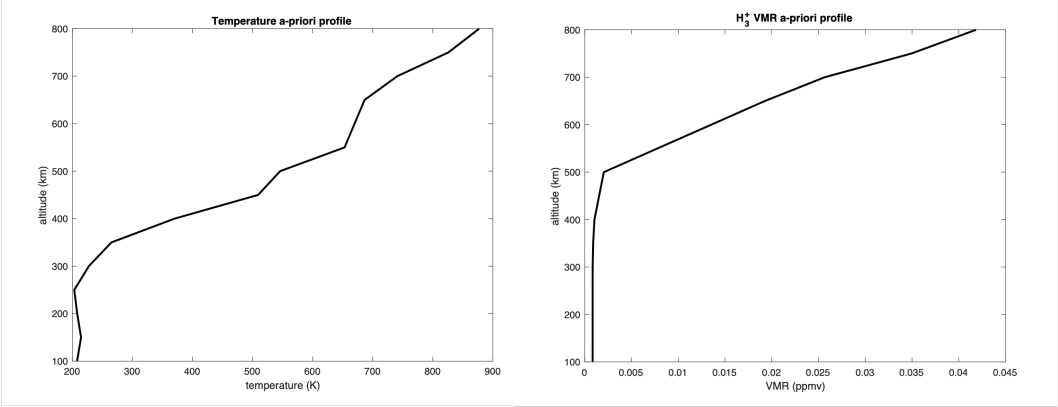

Figure 8. A-priori profiles of temperature (left panel) and H_3^+ VMR (right panel), as from Table 2.

3 Results

3.1 Imager

The band width of the L-band of JIRAM imager covers both CH_4 and H_3^+ emission lines, therefore their signals contribute to produce the observed images. The images clearly show that two well separated layers are present (see for example Figure 1a), one very bright at low altitudes and a fainter one at high altitudes.

Figure 9 shows the radiance map as a function of altitude, obtained by considering only the L-band JIRAM images not contaminated by radiation, listed in Table A1. In this map, each bin has a dimension of 7 deg in latitude and 50 km in altitude. Values falling within each bin are averaged, despite the longitude values. The resolution in altitude varies from a minimum of 4 km to a maximum of 75 km (due to the different resolution among different JIRAM intensity profiles) with an average resolution of 9 km. Errors in the determination of latitude and longitude are ± 1 deg. According to section 2.3, the relative maximum of intensity, located at about 200 km, is clearly due to the CH_4 emission, while the one peaking at about 500 km, can be attributed to H_3^+. CH_4 shows a clear maximum in radiance between 6°N and 18°N, with values decreasing with increasing latitude almost symmetrically with respect to the equator. H_3^+ has a slightly fainter maximum, located at the same latitude. One additional H_3^+ maximum is visible beyond 25°N. The peak altitudes of CH_4 and H_3^+ are also shown as a function of latitude with

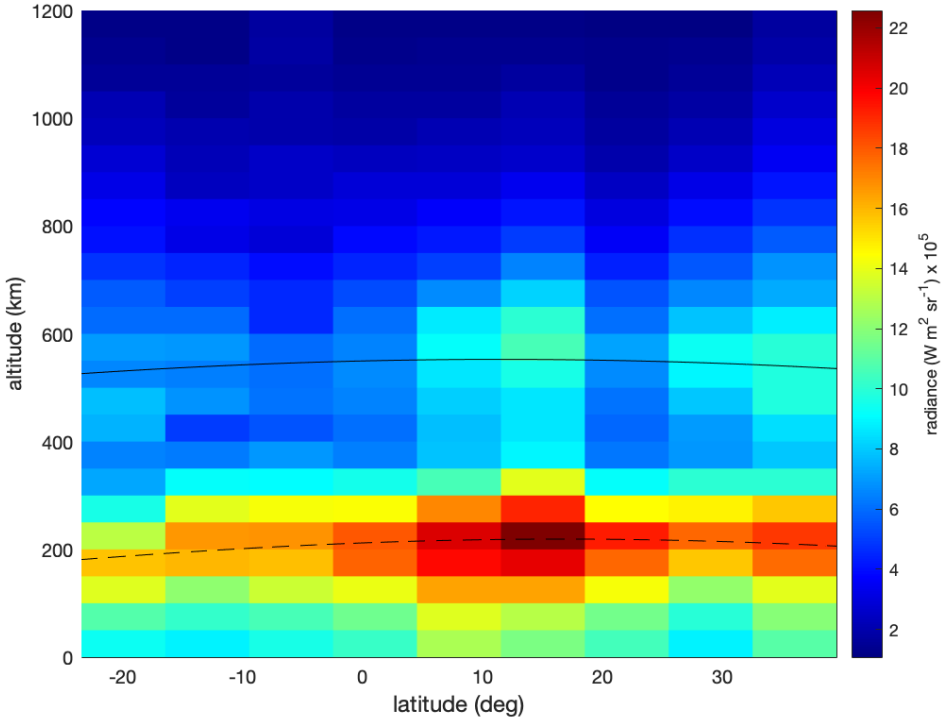

Figure 9. Map of CH_4 and H_3^+ emissions obtained with the L-band images acquired with JIRAM from 21 December 2018 to 3 November 2019. The dashed line indicates the average altitude of the CH_4 peak emission while the solid one provides the average altitude of H_3^+.

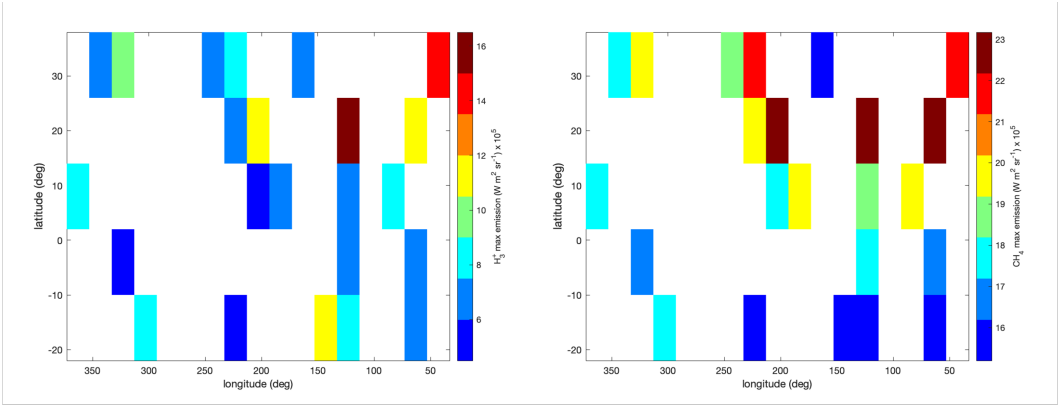

Figure 10. left: Map of H_3^+ emission obtained by considering only the data with a tangent altitude greater than 400 km, acquired with JIRAM-IMA from 21 Dec 2018 to 3 Nov 2019, in terms of longitude and latitude. right: Latitude-longitude distributions of CH_4 emission obtained using the same data, selected for tangent altitudes lower than 400 km.

dashed and solid lines, respectively, obtained as the peak altitude of the maximum of the emission in each latitude bin.

In Figure 10, we report the value of the average intensity measured by JIRAM-IMA in the L-band images listed in Table A1 over the altitude range of H_3^+ (above 400 km, left panel) and of CH_4 (below 400 km, right panel) plotted as a function of latitude and longitude. The maps are obtained by dividing the lat-lon plane in bins of 10° x 20° wide, and averaging the values falling within each bin. A different bin dimension is used for these maps with respect to the one in Figure 9 due to the low coverage in terms of longitude. Despite the sparse measurements, for both molecules we see an area of enhanced emission in the sector from 0° to 160° longitude W mainly concentrated from 9° to 35° latitude North. Higher emissions of CH_4 are present at different locations around the planet, and particularly at about 40-60 W, 120 W and beyond 200 W. Few fainter emissions are observed at lower latitudes, located at about 70 W, 130 W and 200 W. At 40-60 W and 120 W relative maxima of H_3^+, shown in Figure 10 left panel, are observed as well, and one less evident at 310 W. However, since the longitudinal coverage of our measurements is very sparse, any consideration with this parameter is difficult to be explored.

3.2 Retrievals

The results of the analysis of the selected limb spectra with the retrieval code described in section 2.4.1 are reported in Figures 11 to 14. The single limb sequences have been analysed separately, performing three different approaches: first both VMR and temperature were allowed to vary (configuration 1), then only temperature (keeping the VMR fixed at their a-priori values - configuration 2) or VMR (keeping the temperature at Seiff et al. (1998)'s values - configuration 3) have been retrieved. The average temperatures obtained in configuration 1 for the observations in the two separate orbits (21 December 2018 - green line and 27 March 2017 - blue line) are plotted in the left panel of Figure 11, along with the a-priori profile used. We can see in the figure (left panel) that the temperatures obtained from the observations acquired during the two orbits are very similar, therefore we feel that we can discuss the results of the different retrieval configurations merging all the retrieved values in a single plot.

The right panel of Figure 11 shows the comparison of the average temperature profiles obtained with the retrieval configurations 1 and 2. In the 400-800 km altitude range, where H_3^+ peaks, the temperature profiles resulting from the two configurations are different, with a smaller standard deviation in the case of configuration 1. However, in both configurations we find a peak of the temperature at about 550 km, with lower values than the ones reported in Seiff et al. (1998) above 500 km in configuration 1 and above 650 km in configuration 2.

In Figure 12, we compare the maps of the retrieved temperatures for configurations 1 (left panel) and 2 (right panel). The maps have been obtained by merging the observations of the two orbits and averaging the retrieved profiles in bins of 5° in latitude and 150 km in altitude. When H_3^+ VMR is not retrieved, the peak of the emission at 550-600 km is reproduced by an enhancement in the local temperature. In all the three configurations we can reproduce the H_3^+ signal within the measurement error, as it can be seen in Figure 7. Therefore, just using JIRAM limb observations, we cannot conclude if the enhanced signal of H_3^+ in the equatorial region is due to an enhancement of its concentration, of its temperature or both. The results of the retrieval of H_3^+ VMR in configurations 1 and 3 are shown in Figure 13. In both configurations, an enhanced VMR is observed around 10°, but at different altitudes. In case of VMR and T can vary, the maximum of VMR is observed above 650 km, while in case of configuration 3 the maximum of VMR is shifted to lower altitudes.

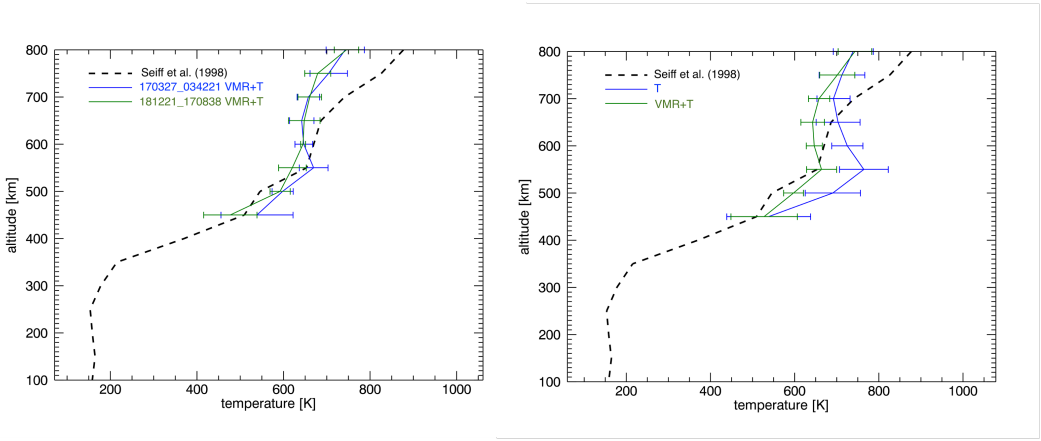

Figure 11. Comparison of the average temperature retrieved in the two considered orbits (left panel) and in retrieval configurations 1 and 2 (right panel). The dashed line represents the a-priori profile taken from Seiff et al. (1998). The error bars represent the standard deviation of the average.

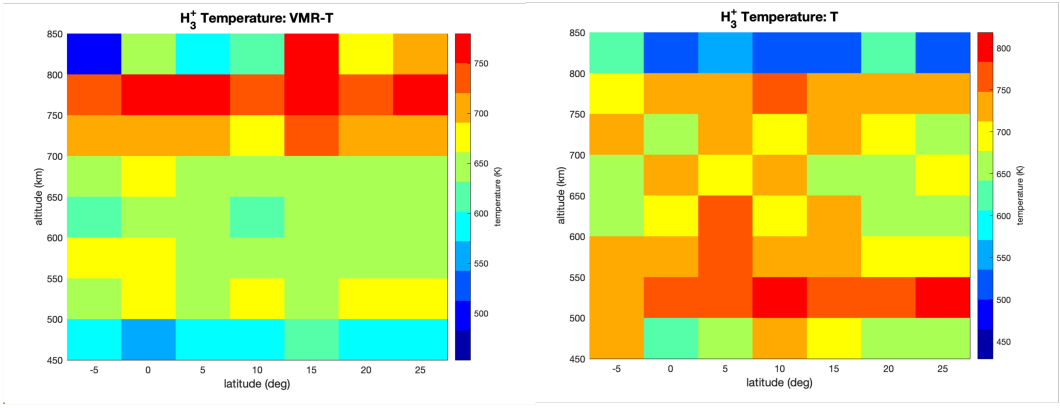

Figure 12. Map of the vertical distribution of H_3^+ temperature as a function of latitude in configuration 1 (left panel) and 2 (right panel).

H_3^+ concentration is shown in Figure 14, for retrieval configurations 1 and 3 respectively. Overall, the distribution of retrieved concentration is similar for the two configurations, and its value decreases with altitude. However, in case of configuration 1 in the retrieval process, the concentration values are higher than in configuration 3 at altitudes from 500 to 650 km.

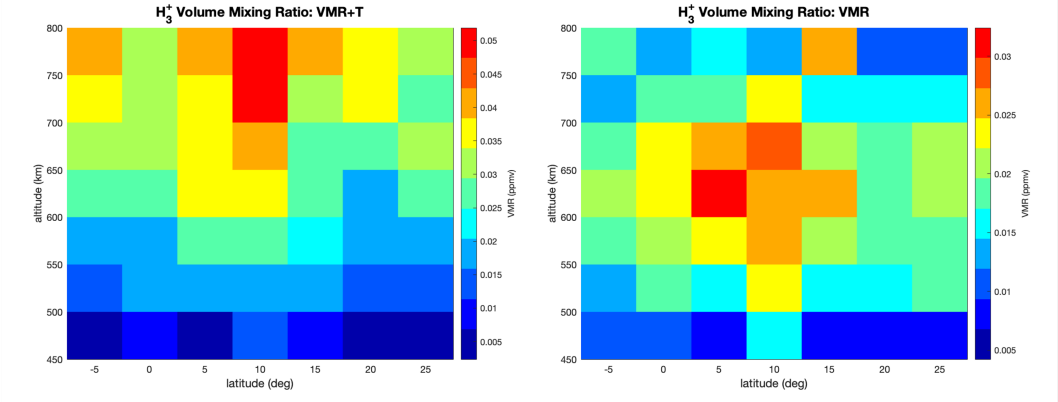

Figure 13. Map of H_3^+ VMR as a function of altitude and latitude, for retrieval configuration 1 (left) and configuration 3 (right).

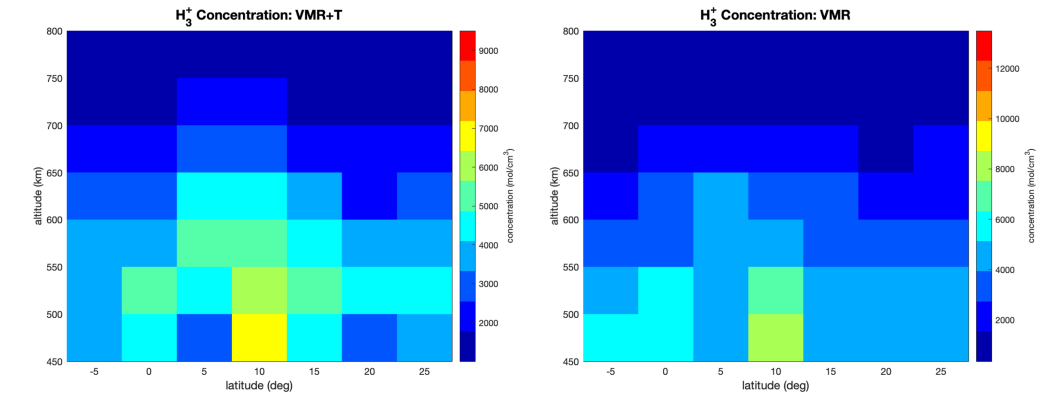

Figure 14. Map of H_3^+ concentration (mol/cm^3) as a function of altitude and latitude, for retrieval configuration 1 (left) and configuration 3 (right)

4 Discussion

The high spatial resolution of JIRAM during the limb observing campaign allowed the simultaneous identification of two emission layers for the first time. Located at about 250 and 600 km, these are compatible with CH_4 and H_3^+ emissions respectively. The spectral capability of JIRAM was used to investigate the zonal and vertical distribution of H_3^+ and the vertical distribution of methane. The maximum enhancements of both CH_4 and H_3^+ are located at about the same latitude, at 6-18°N, as retrieved from the global map in Figure 9. Using only the information provided by the imager it is impossible to distinguish H_3^+ and CH_4 emissions in JIRAM L-band images. Using the information provided by the spectrometer we can conclude that the two species are vertically separated, as shown in Figures 5 and 6. Therefore, we can use the imager data above 400 km to study the H_3^+ contribution, while the data below that altitude can be used to study the methane distribution. The maps in Figure 10 show the distribution of the radiances (in L-band, integrated over the considered altitude range) as a function of latitude and longitude (Figure 10 left panel for H_3^+ and Figure 10 right panel for CH_4). We see that the two molecules have a different distribution of maximum and minimum radiance values. In addition, despite the very patchy longitudinal coverage of JIRAM images, the H_3^+ emission seems to be less intense along the magnetic equator (Connerney et al., 2022), a darkening previously observed in past ground-based observations (Stallard et al., 2018).

Concerning the vertical distribution, we know that the CH_4 emission in the auroral region is expected to occur at 200-300 km, depending on the initial assumptions (Kim et al., 2014). The maximum of the H_3^+ emission has been reported at about 700-900 km and 680-950 km for the H_3^+ overtone and hot overtone in the Northern auroral region (Lystrup et al., 2008; Uno et al., 2014), while an altitude between 300 and 500 km above the 1-bar level has been inferred at mid latitudes from Cassini/VIMS data (Stallard et al., 2015). The radiative transfer code applied to our selected spectral measurements at equatorial latitudes in limb geometry permitted the exploration of VMR, temperature and concentration characteristics of H_3^+. The retrieval of VMR, temperature and concentration of methane deserves a modelling that takes into account the non-LTE condition, as shown in Sànchez-Lòpez et al. (2022). Being not implemented in our retrieval code at the present time, this will be the subject of a future work. The retrieved VMR of H_3^+ has a peak value of about 4.5 x 10^{-2} ppmV, at about 4°N, located at 750 km when temperature and VMR are simultaneously retrieved (configuration 1), while it assumes

a lower value (3 x 10^{-2} ppmV) and is located at lower altitude (550-600 km) if the temperature profile is fixed to the Seiff's values (configuration 3, see Figure 13). In a previous analysis of JIRAM limb measurements, Migliorini et al. (2019) reported a H_3^+ VMR of about 1.4 x 10^{-3} ppmV at 5°N, located close to 600 km. The location of the peak is compatible with the results presented in this work, while the difference in the H_3^+ intensity is due to the changes introduced in the retrieval code to perform this analysis. In addition, values of about 8 x 10^{-4} ppmV at 500 km above the 1-bar level were obtained at 40°S (Migliorini et al., 2019), values that are about 20 times lower than the measurement reported in the equatorial region. Our analysis of JIRAM data indicates that there is an enhancement either in the H_3^+ concentration or in its temperature or in both of them towards the equator, in agreement with the findings in Melin et al. (2014). A higher H_3^+ concentration at the equator compared to mid-latitudes could be partly explained due to smaller solar zenith angles at the equator, which generate more ions through the H_2 solar photoionisation mechanism. However, this process cannot account for an increase factor as high as 20 times. On the other hand, O'Donoghue et al. (2021) shows that the equator is significantly cooler than mid-latitudes, as obtained from H_3^+ temperature, hence temperature effects might be excluded.

Our retrieved values of temperature and VMR are overall in agreement with the revised models for the outer planets (Moore et al., 2019). In addition, an asymmetric distribution of H_3^+ VMR is reported in Migliorini et al. (2019), with higher concentrations in the southern hemisphere above 500 km.

Similarly, oscillations are observed in the retrieved temperature values. H_3^+ temperature has a local maximum at about 600 km either when it is retrieved alone or when also the H_3^+ VMR is retrieved. Its peak value is in the range of 600-800 K, and it is lower than Galileo's measurements above 700 km in both retrieval configurations. However, with the JIRAM data it is not possible to firmly state if oscillations are due to variations in the VMR, temperature or both.

It has been shown that stratospheric oscillations and quasi-quadrennial oscillation occur in the Jovian atmosphere (Cosentino et al., 2017). Temperature anomalies, observed with the Texas Echelon Cross Echelle Spectrograph (TEXES), are well reproduced by the model assuming stochastic waves produced from convection. The observed anomaly progresses also with time, showing a local maximum at the equator in the 2013 data, which

changes into a minimum in the data obtained in late 2014 and beginning of 2015. In O'Donoghue et al. (2016) it is hypothesised that the wavy activity is responsible of the H_3^+ enhancement above the Great Red Spot (GRS). This emission enhancement was explained with acoustic waves resulting from the turbulent troposphere around the GRS, which, after breaking, deposited their energy in the form of heat. The same phenomenon could also be explained with Joule heating, resulting from the GRS vorticity (Ray et al., 2019). Similar effects could occur in the Jupiter's atmosphere and be the cause of the observed features in the JIRAM data reported in our analysis. Recent ground-based observations with Keck II telescope showed a significant and monotonic temperature decrease from the auroral polar regions to the equator that may be explained by redistribution of auroral energy (O'Donoghue et al., 2021). This result comes from the observation of H_3^+ emissions that cover the full disc of Jupiter, from the auroral region to the equator. In particular, observations show a high-temperature planetary-scale structure emanating from the aurora, during a period of enhanced activity. Differently, in our case, local maxima at low latitudes are observed, more compatible with heating due to wavy activity (O'Donoghue et al., 2016).

The presence of an enhanced CH_4 emission layer in the JIRAM data could be in agreement with some wave activity and heat deposition at discrete altitudes or linked to an upwelling mechanism, quite stable with time, although this effect would require a model to quantify and to confirm it. In Cosentino et al. (2017), it is proposed that convection is an important driver for oscillations in gas giant atmospheres. A similar mechanism is observed for other chemical species, like NH_3, retrieved by the MicroWave Radiometer (MRW) onboard Juno (Li et al., 2017) although it sounds a much deeper pressure region (1-60 bars). Ammonia, as well as water, are found to be depleted in the latitudinal band from 40° north to 40° south, with an exception at the equatorial latitudes, where the two species are uniformly mixed (Li et al., 2017, 2020). However, as said, a direct comparison with ammonia cannot be performed because these species are observed at very different pressure levels.

If we explain the JIRAM observations with an enhanced atmospheric layer in the middle stratosphere, possibly at temperatures higher than expected, we require a different disequilibration process than photochemistry. The concept of soft electrons was introduced to explain Jupiter's high exospheric temperature measured on Pioneer 10 and 11 (Hunten, 1977), and may be an alternative to gravity waves or an additional source

of heating. Soft electrons have also been proposed for explaining the hydrogen electroglow in the non-auroral region of the giant planets (e.g. Atreya, 1987). The distribution of soft electron energy deposition in the atmosphere and the excitation of CH_4 would depend on the origin, power spectrum and the angular dependence of the soft electrons, which have been not yet detected. Detailed modelling of this idea is beyond the scope of this paper and could be further tested in a future dedicated work. New observations at limb, planned during the Juno nominal and extended mission, will help extend the observed maps and shed further light on the possible Jovian atmospheric circulation and origin of these detached emission layers.

5 Conclusions

Recent JIRAM measurements allowed the investigation of limb-view emissions of Jupiter's atmosphere in the equatorial region. Limb measurements with the resolution of few km per pixel, as those acquired with JIRAM during these dedicated campaigns, are quite innovative and show a wealth of details never obtained for Jupiter by previous space missions. Dedicated observing campaigns in limb viewing geometry, during orbits 17 to 29 (covering the period December 2018 to September 2020), explored the latitude range 53°S-42°N, and showed for the first time two separate layers due to CH_4 and H_3^+, as seen at limb. We used the limb measurements made by the L-band JIRAM imager to investigate the zonal and vertical distribution of H_3^+ signal and the vertical distribution of CH_4 at equatorial latitudes. The identification of the two layers, made possible by the unique view of JIRAM, represents an important piece of information to refine circulation models. The measurements clearly show for the first time a CH_4 emission layer, located at about 200-300 km above the 1-bar level, directly below the H_3^+ layer where emissions are observed at about 500-600 km. H_3^+ spectral signatures can be reproduced by retrieving either the temperature vertical profile or the vertical distributions of its VMR and temperature simultaneously, while CH_4 will be studied in a future work to include the non-LTE condition. In the vertical region above 400 km, the resulting T profile shows a peak at about 550 km that is higher in the case the VMRs are kept fixed in the retrieval process. Our analysis indicates differences in the thermal structure compared to the results obtained with the Galileo probe, potentially revealing significant variability in the exospheric temperature with time. The H_3^+ VMR distribution is similar in the considered cases, but the peak shifts towards higher altitudes and has a

higher value in the configuration where VMR and T can vary in the retrieval process. From these results, it is not possible to firmly conclude if the observed H_3^+ features are due to a real increase of their VMRs or rather to variation of temperature, because the retrieval procedure is able to reproduce JIRAM data in all retrieval configurations.

Here we speculate that vertically propagating waves are the most plausible explanation to describe the VMR and/or temperature variations of H_3^+ at mid and equatorial latitudes in the JIRAM data, in analogy with previous observations (Cosentino et al., 2017; O'Donoghue et al., 2016).

We can also speculate that soft electron precipitation might cause the observed CH_4 signal, in analogy with previous explanations to the Pioneer measurements of the high exosphere of Jupiter (Hunten, 1977), and the electroglow at the giant planets (e.g. Atreya, 1987). However, more accurate modelling of magnetospheric and electronic precipitation is required to confirm this hypothesis. The characterisation of CH_4 and H_3^+ species, simultaneously observed with JIRAM, is finally important for better constraining the atmospheric models of Jupiter and a better comprehension of the circulation of these species.

6 Open Research

The calibrated JIRAM data used for this work are available at the NASA Planetary Data System website and described in (Noschese & Adriani, 2017; Adriani et al., 2017a). The Maps in Figure 4 was produced by using the commercial software ENVI (`https://www.harrisgeospatial.com/Software-Technology`). The analysis has been done using homemade procedure based on IDL and Fortran languages. Data products of this work are reported in (Dinelli, 2021).

Acknowledgments

The JIRAM project is funded by the Italian Space Agency (ASI). In particular, this work has been developed under the agreement 2016-23-H.0

Appendix A List of JIRAM-IMA data used for this research

Table A1. List of JIRAM images (JIRAM-IMA) used in the present investigation. The column 'Observation' identifies the image name (as it is reported in the PDS archive), while the ranges of System III planetocentric geographycal latitude (in deg) and longitude (in deg), are reported in columns 2 and 3.

Observation	Latitude range	Longitude range
JM0171		
JIR-IMG-EDR-2018355T165044-V01.IMG	15.0795N-25.6026N	223.3481-228.7901
JIR-IMG-EDR-2018355T165717-V01.IMG	4.1836N-13.2026N	209.3811-212.2929
JIR-IMG-EDR-2018355T170149-V01.IMG	6.2586S-2.3903S	199.7330-200.3485
JIR-IMG-EDR-2018355T170545-V01.IMG	0.7353N-2.5613N	174.7923-182.0536
JM0181		
JIR-IMG-EDR-2019043T172119-V01.IMG	23.7105N-36.2755N	157.8081-165.5014
JIR-IMG-EDR-2019043T173748-V01.IMG	, 5.9681S-1.5688S	117.8844-119.2543
JIR-IMG-EDR-2019043T183143-V01.IMG	36.3001S-13.7663S	102.8070-115.5961
JIR-IMG-EDR-2019043T185147-V01.IMG	47.7705S-21.4223S	111.3855-128.1595
JM0201		
JIR-IMG-EDR-2019149T081603-V01.IMG	14.0825N-23.2032N	325.8294-333.6507
JIR-IMG-EDR-2019149T085707-V01.IMG	20.7363S-1.6725S	308.6906-316.2082
JIR-IMG-EDR-2019149T091726-V01.IMG	32.2032S-8.9053S	306.1715-318.6140
JIR-IMG-EDR-2019149T092230-V01.IMG	34.6397S-10.7575S	305.5659-318.7391
JM0211		
JIR-IMG-EDR-2019202T040443-V01.IMG	5.0535S-4.2361N	65.7260-71.9941
JIR-IMG-EDR-2019202T052644-V01.IMG	44.2991S-15.3318S	45.1409-60.6679
JIR-IMG-EDR-2019202T053415-V01.IMG	47.1793S-17.9849S	47.9021-66.7939
JM0221		
JIR-IMG-EDR-2019255T033541-V01.IMG	8.0070N-17.2354N	50.3231-54.8906
JIR-IMG-EDR-2019255T033811-V01.IMG	2.9783N-12.6342N	43.6693-46.9465
JIR-IMG-EDR-2019255T043502-V01.IMG	16.4530S-1.0814S	342.7394-349.7376
JIR-IMG-EDR-2019255T044233-V01.IMG	27.5683S-4.1084S	345.8359-355.9748
JIR-IMG-EDR-2019255T045133-V01.IMG	33.6485S-9.6321S	0.0006-359.9998
JM0231		
JIR-IMG-EDR-2019307T221639-V01.IMG	11.4622N-18.2561N	182.4169-187.4077
JIR-IMG-EDR-2019307T222207-V01.IMG	4.0851S-1.6180N	165.9429-167.4344
JM0241		
JIR-IMG-EDR-2019360T172532-V01.IMG	23.2495N-33.2145N	321.2914-329.4380
JIR-IMG-EDR-2019360T173036-V01.IMG	17.4570N-25.5591N	306.7894-313.9234
JM0251		
JIR-IMG-EDR-2020048T173525-V01.IMG	30.4268N-41.9685N	281.1528-290.2075
JIR-IMG-EDR-2020048T174458-V01.IMG	25.8754N-32.9970N	247.4178-257.9277
JIR-IMG-EDR-2020101T135904-V01.IMG	27.7355S-18.8677S	298.3254-302.1651
JIR-IMG-EDR-2020101T140337-V01.IMG	40.6497S-31.6756S	300.2135-308.8700
JM0271		
JIR-IMG-EDR-2020154T100651-V01.IMG	35.4718N-45.4150N	70.6816-83.2845
JIR-IMG-EDR-2020154T101524-V01.IMG	31.3732N-34.7915N	39.4754-50.6786
JIR-IMG-EDR-2020154T102056-V01.IMG	23.4125N-24.6931N	26.1395-34.8305
JIR-IMG-EDR-2020154T111709-V01.IMG	50.3844S-32.9904S	33.7651-50.9187
JM0281		
JIR-IMG-EDR-2020207T060208-V01.IMG	33.9678N-44.2826N	159.5375-170.6685
JIR-IMG-EDR-2020207T062041-V01.IMG	5.8582N-9.4193N	109.1268-118.0512
JIR-IMG-EDR-2020207T071052-V01.IMG	43.5353S-24.7151S	106.9207-127.4483
JIR-IMG-EDR-2020207T071553-V01.IMG	47.0992S-26.4510S	110.4395-130.2419
JIR-IMG-EDR-2020207T073125-V01.IMG	52.8392S-30.0824S	124.0210-139.2670
JM0291		
JIR-IMG-EDR-2020260T020248-V01.IMG	30.9891N-38.3766N	229.0602-239.6824
JIR-IMG-EDR-2020260T021220-V01.IMG	16.7883N-19.1789N	206.0570-213.1100
JIR-IMG-EDR-2020260T033207-V01.IMG	51.4122S-27.7863S	206.5596-222.2353

References

Acton, C. H. (1996). Ancillary data services of nasa's navigation and ancillary information facility. *Planetary and Space Science*, *44*(1), 65-70. doi: 10.1016/0032-0633(95)00107-7

Adriani, A., Filacchione, G., Di Iorio, T., & et al. (2017a). Jiram, the jovian infrared auroral mapper. *Space Science Reviews*, *213*, 393. doi: 10.1007/s11214-014-0094-y

Adriani, A., Mura, A., Moriconi, M., & et al. (2017b). Preliminary jiram results from juno polar observations: 2. analysis of the jupiter southern h_3^+ emissions and comparison with the north aurora. *Geophysical Research Letters*, *44*. doi: 10.1002/2017GRL072905

Altieri, F., Dinelli, B., Migliorini, A., & et al. (2016). Mapping of hydrocarbons and h_3^+ emissions at jupiter's north pole using galileo/nims data. *Geophysical Research Letters*, *43*, 11558 - 11566. doi: 10.1002/2016GL070787

Atreya, S. K. (1987). Atmospheres and ionospheres of the outer planets and their satellites. In (p. 47-48). Springer, New York-Heidelberg.

Ballester, G. E., Miller, S., Tennyson, J., Trafton, L., & Geballe, T. (1994). Latitudinal temperature variations of jovian h_3^+. *Icarus*, *107*, 189-194.

Bonfond, B., Gladstone, G., Grodent, D., Greathause, T., Versteeg, M., Hue, V., & et al. (2017). Morphology of the uv aurorae jupiter during juno's first perijove observations. *Geophysical Research Letters*, *44*, 4463-4471. doi: 10.1002/2017GL073114

Bougher, S., Waite, J., Majeed, T., & Gladstone, G. (2005). Jupiter thermospheric general circulation model (jtgcm): Global structure and dynamics driven by auroral and joule heating. *Journal of Geophysical Research: Planets*, *110*, E04008.

Caldwell, J., Halthore, R., Orton, G., & Berstralh, J. (1988). Infrared polar brightenings on jupiter vi. spatial properties of methane emission. *Icarus*, *74*, 331-339.

Caldwell, J., Tokunags, A., & Orton, G. (1983). Further observations of 8-μm polar brightenings of jupiter. *Icarus*, *53*, 133-140.

Carlotti, M. (1988). Global-fit approach to the analysis of limb-scanning atmospheric measurements. *Applied Optics*, *27*, 3250-3254.

Clarke, J., Ajello, J., Ballester, G., & et al. (2002). Ultraviolet emissions from the magnetic footprints of io, ganymede, and europa on jupiter. *Nature*, *415*, 997-1000.

Connerney, J., Baron, R., Satoh, T., & Owen, T. (1993). Images of excited h_3^+ at the foot of the io flux tube in jupiter's atmosphere. *Science*, *262*, 1035-1038.

Connerney, J., Timmins, S., Oliversen, R., & et al. (2022). A new model of jupiter's magnetic field at the completion of juno's prime mission. *Journal of Geophysical Research: Planets*, *127*. doi: doi.org/10.1029/2021JE007138

Cosentino, R., Morales-Juberias, R., Greathouse, T., Orton, G., Johnson, P., Fletcher, L., & Simon, A. (2017). New observations and modeling of jupiter's quasi-quadrennial oscillation. *Journal of Geophysical Research*, *122*, 2719-2744. doi: 10.1002/2017JE005342

Dinelli, B. (2021). Ch_4 and h_3^+ retrieval results [data set]. *Zenodo*. doi: https://doi.org/10.5281/zenodo.5658387

Dinelli, B., Adriani, A., Mura, A., Altieri, F., Migliorini, A., & Moriconi, M. L. (2019). Juno/jiram's view of jupiter's h_3^+ emissions. *Philosophical Transaction of the Royal Society A*, *377*. doi: 10.1098/rsta.2018.0406

Drossart, P., Bezard, B., Atreya, S., & et al. (1993). Thermal profiles in the auroral regions of jupiter. *Journal of Geophysical Research*, *98*, 18803-18812. doi: 10.1029/93JE01801

Drossart, P., Maillard, J.-P., Cladwell, S., & et al. (1989). Detection of the h_3^+ on jupiter. *Nature*, *340*, 539-541. doi: 10.1038/340539a0

Gèrard, J.-C., Mura, A., Bonfond, B., Gladstone, G., Adriani, A., Hue, V., ... Levin, S. (2018, 04). Concurrent ultraviolet and infrared observations of the north jovian aurora during juno's first perijove. *Icarus*, *312*. doi: 10.1016/j.icarus.2018.04.020

Giles, R., Fletcher, L., Irwin, P., & et al. (2016). Detection of h_3^+ auroral emission in the jupiter's 5-micron window. *Astronomy and Astrophysics*, *589*, A67. doi: 10.1051/0004-6361/201628170

Grodent, D., Waite, J. J., & Gèrard, J. (2001). A self-consistent model of the jovian auroral thermal structure. *Journal of Geophysical Research*, *106*, 12933-12952. doi: 10.1029/2000JA900129

Hunten, A. J., D.M.and Dessler. (1977). Soft electrons as a possible heat source for

jupiter's thermosphere. *Planetary and Space Science*, *25*, 817-821.

Kim, S., Caldwell, J., Rivolo, A., Wagener, R., & Orton, G. (1985). Infrared polar brightening on jupiter iii. spectrometry from the voyager 1 iris experiment. *Icarus*, *64*, 233-248. doi: 10.1016/0019-1035(85)90088-0

Kim, S., Drossart, P., Caldwell, J., & et al. (1991). Images of aurorae on jupiter from h_3^+ emission at 4 μm. *Nature*, *353*, 536-539. doi: 10.1038/353536a0

Kim, S., Geballe, T., Seo, H., & Jim, J. (2009). Jupiter's hydrocarbon polar brightening: Discovery of 3-micron line emission from south polar ch_4, c_2h_2 and c_2h_6. *Icarus*, *202*, 354-357. doi: 10.1016/j.icarus.2009.03.020

Kim, S., Sim, C., Ho, J., & et al. (2015). Hot ch_4 in the polar regions of jupiter. *Icarus*, *257*, 217-220. doi: 10.1016/j.icarus.2015.05.008

Kim, S., Sim, C., Sohn, M., & Moses, J. (2014). Ch_4 mixing ratios at microbar pressure levels of jupiter a constrained by 3-micron iso data. *Icarus*, *237*, 42-51. doi: 10.1016/j.icarus.2014.04.023

Kita, H., Fujisawa, S., Tao, C., & et al. (2018). Horizontal and vertical structures of jovian infrared aurora: Observations using subaru ircs with adaptive optics. *Icarus*, *313*, 93-106.

Koskinen, T., Aylaward, A., & Miller, S. (2007). A stability limit for the atmospheres of giant extrasolar planets. *Nature*, *412*, 891.

Li, C., Ingersoll, A., Bolton, S., Levin, S., Janssen, M., Atreya, S., & et al. (2020). The water abundance in jupiter's equatorial zone. *Nature Astronomy*, *4*, 609-616. doi: 10.1038/s41550-020-1009-3

Li, C., Ingersoll, A., Janssen, M., & et al. (2017). The distribution of ammonia on jupiter from a preliminary inversion of juno microwave radiometer data. *Geophysical Research Letters*, *44*, 5317-5325. doi: 10.1002/2017GL073159

Lindsay, C., & McCall, B. (2001). Comprehensive evaluation and compilation of h_3^+ spectroscopy. *Journal of Molecular Spectroscopy*, *210*(1), 60-83. doi: https://doi.org/10.1006/jmsp.2001.8444

Lystrup, M., Miller, S., Dello Russo, N., Vervack, R., & Stallard, T. (2008, apr). First vertical ion density profile in jupiter's auroral atmosphere: Direct observations using the keck II telescope. *The Astrophysical Journal*, *677*(1), 790–797. doi: https://doi.org/10.1086/529509

Marten, A., De Bergh, C., Owen, T., Gautier, D., Maillard, J., Drossart, P., ... Or-

ton, G. (1994). Four micron high-resolution spectra of jupiter in the north equatorial belt: H_3^+ emissions and the 12c/13c ratio. *Planetary and Space Science*, *42*(5), 391-399. doi: https://doi.org/10.1016/0032-0633(94)90128-7

Melin, H., Miller, S., Stallard, T., & Grodent, D. (2005). Non-lte effects on h_3^+ emission in the jovian upper atmosphere. *Icarus*, *178*(1), 97-103. doi: https://doi.org/10.1016/j.icarus.2005.04.016

Melin, H., Stallard, T., O'Donoghue, J., Badman, S., & Miller, S. (2014). On the anticorrelation between h_3^+ temperature and density in giant planet ionospheres. *MNRAS*, *438*, 1611-1617. doi: https://doi.org/10.1093/mnras/stt2299

Migliorini, A., Dinelli, B., Moriconi, M., Altieri, F., Adriani, A., Mura, A., & et al. (2019). H_3^+ characteristics in the jupiter atmosphere as observed at limb with juno/jiram. *Icarus*, *329*, 132-139. doi: https://doi.org/10.1016/j.icarus.2019.04.003

Miller, S., Achilleos, N., Ballester, G. E., Lam, H. A., Tennyson, J., Geballe, T. R., & Trafton, L. M. (1997). Mid-to-low latitude h_3^+ emission from jupiter. *Icarus*, *130*(1), 57-67. doi: https://doi.org/10.1006/icar.1997.5813

Miller, S., Joseph, R. D., & Tennyson, J. (1990). Infrared emissions of h_3^+ in the atmosphere of jupiter in the 2.1 and 4.0 micron region. *Astrophysical Journal Letter*, *360*, L55. doi: https://doi.org/10.1086/185811

Miller, S., Tennyson, J., Geballe, T. R., & Stallard, T. (2020, Aug). Thirty years of h_3^+ astronomy. *Rev. Mod. Phys.*, *92*, 035003. doi: 10.1103/RevModPhys.92.035003

Moore, L., Melin, H., O'Donoghue, J., Stallard, T. S., Moses, J. I., Galand, M., ... Schmidt, C. A. (2019). Modelling h_3^+ in planetary atmospheres: effects of vertical gradients on observed quantities. *Philosophical Transactions of the Royal Society A: Mathematical, Physical and Engineering Sciences*, *377*(2154), 20190067. doi: 10.1098/rsta.2019.0067

Moriconi, M., Adriani, A., Dinelli, B., & et al. (2017). Preliminary jiram results from juno polar observations: 3. evidence of diffuse methane presence in the jupiter auroral regions. *Geophysical Research Letters*, *44*, 4641-4648. doi: 10.1002/2017GL073592

Mura, A., Adriani, A., Altieri, F., & et al. (2017). Infrared observations of jovian aurora from juno's first orbit: main oval and satellite footprints. *Geophysical Re-*

search Letters, *44*. doi: 10.1022/2017GRL072954

Mura, A., Adriani, A., Altieri, F., & et al. (2018). Juno observations of spot structures and a split tail in io-induced aurorae on jupiter. *Science*, *361*, 774-777. doi: 10.1126/science.aat1450

Noschese, R., & Adriani, A. (2017). Juno jupiter jiram raw data archive v1.0. nasa planetary data system.
doi: 10.17189/FAY5-DE13

O'Donoghue, J., Moore, L., Bhakyapaibul, T., Melin, H., Stallard, T., Connerney, J., & Tao, C. (2021). Global upper-atmospheric heating on jupiter by the pola auroraeheating of jupiter's upper atmosphere above the great red spot. *Nature*, *596*, 54-67. doi: 10.1038/s41596-021-03706-w

O'Donoghue, J., Moore, L., Stallard, T., & Melin, H. (2016). Heating of jupiter's upper atmosphere above the great red spot. *Nature*, *536*, 190-192. doi: 10.1038/nature18940

Ray, L., Lorch, C., O'Donoghue, J., Yates, J., Badman, S., Smith, C., & Stallard, T. (2019). Why is the h_3^+ hot spot above jupiter's great red spot so hot? *Philosophical Transaction of the Royal Society A*, *377*. doi: 10.1098/rsta.2018.0407

Rodgers, C. D. (2000). *Inverse methods for atmospheric sounding*. WORLD SCIENTIFIC. doi: 10.1142/3171

Sada, P., Jennings, D., Romani, P., Bjoraker, G., Flasar, F., Kunde, V., ... McCabe, G. (2003, 05). Transient ir phenomena observed by cassini/cirs in jupiter's auroral regions. *Bulletin of the American Astronomical Society*, *35*, 402.

Sànchez-Lòpez, A., Lòpez-Puertas, M., Garcìa-Comas, M., Funke, B., Fouchet, T., & Snellen, I. (2022). The ch_4 abundance in jupiter's upper atmosphere. *Astronomy and Astrophysics*, *662*, A91.

Satoh, T., & Connerney, J. (1999). Jupiter h_3^+ emissions viewed in corrected jovimagnetic coordinates. *Icarus*, *141*, 236-252. doi: 10.1006/icar.1999.6173

Seiff, A., Kirk, D. B., Knight, T. C. D., Young, R. E., Mihalov, J. D., Young, L. A., ... Atkinson, D. (1998). Thermal structure of jupiter's atmosphere near the edge of a 5-μm hot spot in the north equatorial belt. *Journal of Geophysical Research*, *103*, 22857-22889. doi: 10.1029/98JE01766

Sinclair, J., Orton, G., Fernandes, J., & et al. (2019). A brightening of jupiters auroral 7.8-μm ch_4 emission during a solar-wind compression. *Nature Astron*, *3*, 607613. doi: 10.1038/s41550-019-0743-x

Sinclair, J. A., Orton, G., Greathouse, T., Fletcher, L., Tao, C., & et al. (2017). Independent evolution of stratospheric temperatures in jupiters northern and southern auroral regions from 2014 to 2016. *Geophysical Research Letters*, *44*, 53455354. doi: 10.1002/2017GL073529

Stallard, T., Burrell, A., Melin, H., & et al. (2018). Identification of jupiter's magnetic equator within h_3^+ ionospheric emission. *Nature Astronomy*, *2*, 773-777. doi: 10.1038/s41550-018-0523-z

Stallard, T., Melin, H., Miller, S., & et al. (2015). Cassini vims observations of h_3^+ emission on the nightside of jupiter. *Journal of Geophysical Research: Space Physics*, *120*, 6948-6973. doi: 10.1002/2015JA021097

Stallard, T., Melin, H., Miller, S., Moore, L., J., O., Connerney, J., & et al. (2017). The great cold spot in jupiter's upper atmosphere. *Geophysical Research Letters*, *44*, 3000. doi: 10.1002/2016GL071956

Tao, C., Badman, S., & Fujimoto, M. (2011). Uv and ir auroral emission model for the outer planets: Jupiter and saturn comparison. *Icarus*, *213*, 581-592. doi: 10.1016/j.icarus.2011.04.001

Uno, T., Yasaba, Y., Tao, C., & et al. (2014). Vertical emissivity profiles of jupiter's northern h_3^+ and h_2 infrared auroras observed by subaru/ircs. *Journal of Geophysical Research Space Physics*, *119*, 1021910241. doi: 10.1002/2014JA020454